7.1 Introduction

The phosphors are generally used in the optical device applications including flat panel display device like field emission display (FEDs), plasma display panels (PDPs) and thin film electroluminescent devices (TFEL) [131, 182]. Due to these technological applications, efforts have been made to discover the novel host materials as well as activators to improve the performance of the phosphors. Oxide based phosphors are more practical and attractive than traditional sulphides and halides due to their resistance to moisture [131]. Among the various phosphor materials, the alkaline earth stannates M_2SnO_4: M= Ca, Sr, Ba the Sr_2SnO_4 have drawn more attention as host material for phosphor applications because of its wide band gap (i.e., direct band gap 4.6 eV and indirect band gap 4.2 eV) [172], stable crystal structure and high physical and chemical stability [131]. The photoluminescence properties of lanthanides doped Sr_2SnO_4 have been studied extensively for various applications including white light emitting diode [54]. The white light emitting diode (LED) is essential part of human life, which is efficiently excited by the photon from visible, near ultraviolet (NUV) and ultraviolet (UV) region is the critical material of the LED producing. It is reported in the literature that Eu^{3+} doped $Sr_{2-x}Eu_xSnO_4$ have shown red and orange emission [187]. On extensive literature survey it is found that the Eu has been incorporated at Sr site of Sr_2SnO_4 [133, 137, 182]. To the best of our knowledge no reports are available on the Eu incorporated at the Sn site of Sr_2SnO_4. The difference in the ionic radii of Sn^{4+} and Eu^{3+} in six coordination states is approximately ± 25 %. Therefore, according to Hume-Rothery condition Eu has a substitute for Sn site.

In this Chapter, effect of Eu^{3+} doping (on Sn^{4+} site) on structural optical properties of Sr_2SnO_4 has been discussed.

7.2 Results and Discussions

In present discussion, the system $Sr_2Sn_{1-x}Eu_xO_4$ is abbreviated as SSE and the compositions with x=0, 0.01, 0.02, 0.04, 0.06 and 0.10 of this system are abbreviated as SSE0, SSE1, SSE2, SSE4, SSE6 and SSE10 throughout the discussion of the results.

7.2.1 X-ray diffraction analysis

The X-ray diffraction analysis of synthesized samples has been carried out to identify the phases present in the sample. Figure 7.1(a) shows the X-ray diffraction pattern of the samples. All observed peaks are well matched with COD-1539931 available for undoped sample Sr_2SnO_4. Absence of any extra peak or secondary phase corresponds to raw materials $SrCO_3$, SnO_2 and Eu_2O_3 indicate the complete solubility of Eu^{3+} at Sn^{4+} site in Sr_2SnO_4 within investigated compositional range. Further to insure the incorporation of Eu^{3+} at Sn^{4+} site, magnified view of intense XRD peaks corresponding to plane (103) and (110) are shown in Figure 7.1(b). A systematic shift towards lower angle side is noticed for Eu doped samples. Since the ionic radii of Eu^{3+} in sixth coordination number is 0.95 Å, larger than ionic radii of Sn^{4+} in same coordination number (0.69 Å). The shift in position of XRD peaks towards lower angle side confirms incorporation of Eu^{3+} at Sn^{4+} site.

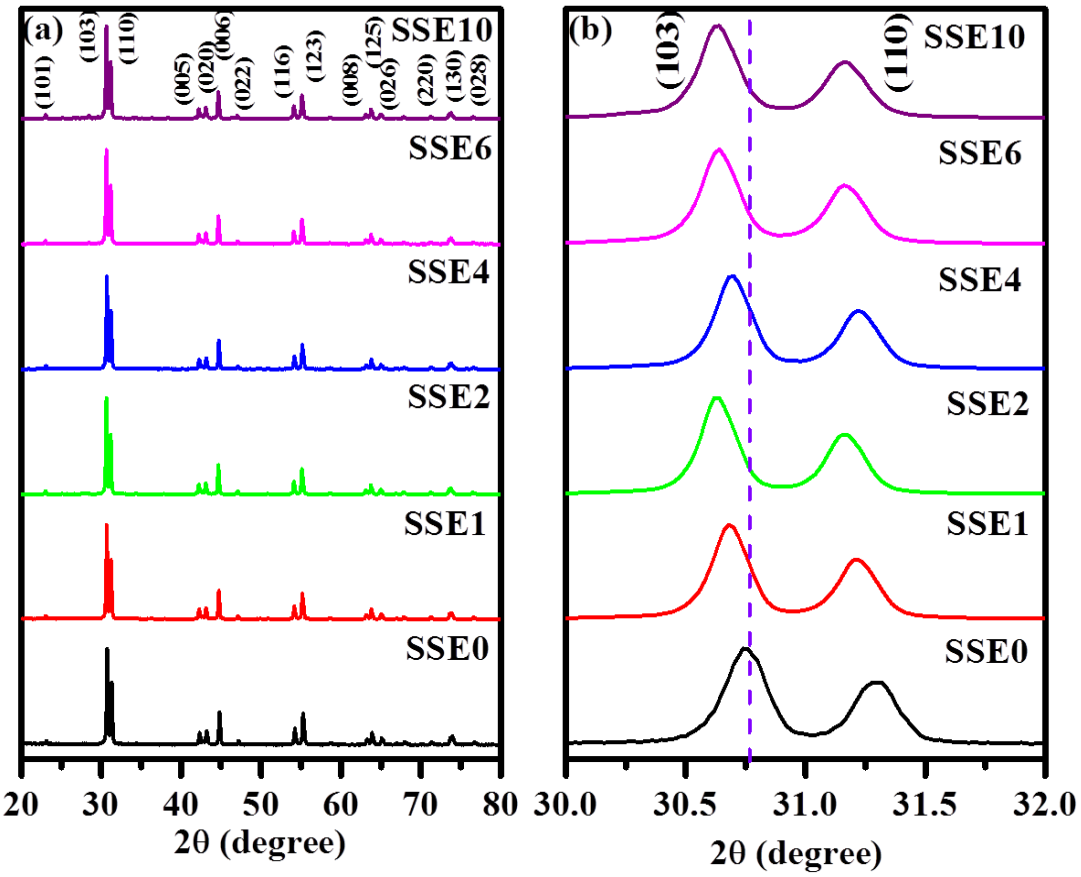

Figure 7.1 (a) X-ray diffraction pattern of all samples (b) Enlarged view of peak (103) & (110).

The Reitveld refinement of the XRD pattern of all the samples have been carried out using "**FullProf**" software and shown in Figure 7.2(a). For refinement process tetragonal crystal structure and space group I4/mmm similar to Sr_2SnO_4 are considered. The refinement processes are already discussed in Chapter 3. Structural parameters along with reliability parameters obtained from the refinement are given in Table 7.1. From Table 7.1, it is observed that the value of lattice parameters of Eu^{3+} in the solid solution $Sr_2Sn_{1-x}Eu_xO_4$ (a=b) increases, while c- parameter decreases with Eu^{3+} concentration. To understand this variation, the structure of sample SSE4 generated using Vesta software is shown in Figure 7.2(b). In the structure of Sr_2SnO_4, number of Sn-sites per unit volume along a/b axis is more as compared to c axis. Thus, possibility of presence of Eu ion at Sn site along a and b axis is more as

compared to c-axis. Hence, increase in the lattice parameter a and b is more as compared to c-axis are observed.

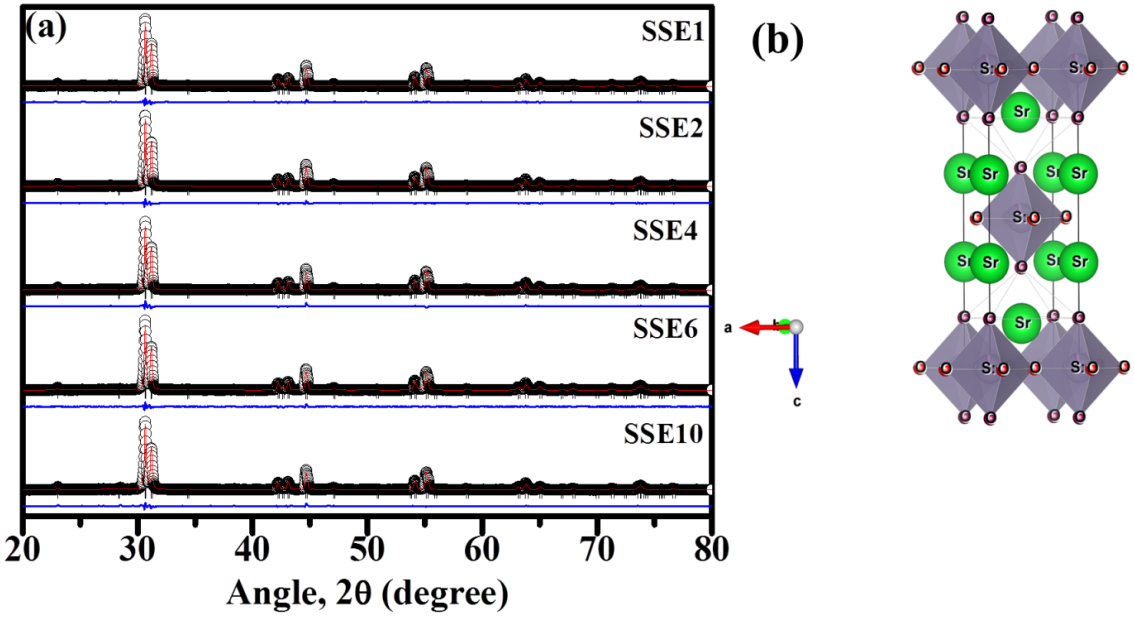

Figure 7.2 (a) Rietveld refinement pattern of Eu-doped samples (b) Unit Cell of a sample SSE4 generated by VESTA software.

The broadening in the X-ray diffraction peaks have contribution of various factors like crystallite size, lattice strain, instrumental broadening, etc. After correction the instrumental broadening from full width at half maxima (FWHM) of most intense peak (013), it is used to calculate the crystallite size using Eq. (2.15). Obtained value of crystallite size for all samples are given in Table 7.1. From Table 7.1, it is observed that value of crystallite size of all the samples is larger compared to undoped sample Sr_2SnO_4. Bernard Jaffe et al. have reported that donors inhibit the grain growth formation while acceptors are promote grain growth formation in perovskite oxides [23]. The Eu^{3+} at Sn^{4+} site is an acceptor $(Eu)'_{Sn}$ therefore, higher value of crystallite size in present sample is consistent with results of earlier workers. Further, doping of Eu^{3+} at Sn^{4+} site, charge compensation is expected according to Eq. (7.1).

$$Eu_2O_3 \xrightarrow{2Sr_2SnO_4} 4Sr_{Sr}{}^{x} + 2Eu_{Sn}{}' + V_{\ddot{O}} \qquad (7.1)$$

Oxygen vacancies in many oxide ceramics have favoured grain growth, therefore in these samples also oxygen vacancies may also be responsible for the larger crystallite size of doped sample [23].

Table 7.1 Structural parameters obtained from Rietveld Refinement of all samples.

Parameters	SSE0	SSE1	SSE2	SSE4	SSE6	SSE10
Lattice Parameters						
a=b	4.05084(6)	4.05448(5)	4.05495(9)	4.05478(5)	4.05551(4)	4.055502(8)
c	12.59040(18)	12.58872(11)	12.59010(11)	12.58710(13)	12.58950(13)	12.58960(14)
Angle (α,β,γ)	90=90=90	90=90=90	90=90=90	90=90=90	90=90=90	90=90=90
R_{wp}	20.4	9.36	9.31	10.5	10.9	13.2
R_p	16.7	9.22	8.82	10.4	10.5	12.3
χ^2	4.17	3.16	3.48	3.98	3.23	3.39
R_{Bragg}	3.4327	2.253	1.826	3.92	2.781	2.382
$S=R_{wp}/R_p$	1.221556886	1.015184382	1.055555556	1.009615385	1.038095238	1.073170732
Atomic Coordinate						
Sr	(0,0,0.35267)	(0,0,0.35236)	(0,0,0.35204)	(0,0,0.35252)	(0,0,0.35350)	(0,0,0.35300)
Sn	(0,0,0)	(0,0,0)	(0,0,0)	(0,0,0)	(0,0,0)	(0,0,0)
Eu	(0,0,0)	(0,0,0)	(0,0,0)	(0,0,0)	(0,0,0)	(0,0,0)
O1	(0.5,0,0)	(0.5,0,0)	(0.5,0,0)	(0.5,0,0)	(0.5,0,0)	(0.5,0,0)
O2	(0,0,0.15754)	(0,0,0.16198)	(0,0,0.16318)	(0,0,0.16578)	(0,0,0.15350)	(0,0,0.15300)
Atomic Occupancy						
Sr	2.00122	2.01382	2.01053	2.01611	2.01024	2.01323
Sn	1.00125	0.99077	0.98073	0.96025	0.9426	0.89728
Eu	0	0.00923	0.01927	0.03975	0.0574	0.10272
O1	2.04861	2.00318	1.81438	1.7642	1.65565	1.65739
O2	1.95139	1.84079	1.80072	1.8542	1.85199	2.0343
Bond Length						
Sr-Sn (along a,b)	3.41255(3)	3.416631(4)	3.41928(6)	3.41565(8)	3.40958(9)	3.41271(6)
Sr-Sn (along c)	4.44015(15)	4.43575(11)	4.43222(11)	4.43720(5)	4.45039(5)	4.44413(15)
Sn-O1 (along a,b)	2.02538(4)	2.02718(4)	2.02748(6)	2.02739(4)	2.02776(4)	2.02751(7)
Sn-O2 (along c)	1.98344(7)	2.03912(5)	2.05445(5)	2.08669(6)	1.93249(7)	1.92621(8)
Bond Angle						
O1-Sr-O1	95.0314	94.9686	94.8468	95.0435	95.4233	95.2216
O2-Sr-O2	174.8608	172.7939	172.3532	170.8136	176.4796	176.9819
Crystallite Size (nm)	49.30	55.63	57.89	62.24	66.95	69.59
$I_{02}\frac{(^5_0D\rightarrow^7_0F)}{(^5_0D\rightarrow^7_2F)}$	--	0.13	0.75	0.95	1.06	0.98
$I_{12}\frac{(^5_0D\rightarrow^7_1F)}{(^5_0D\rightarrow^7_2F)}$	--	0.19	0.15	0.14	0.11	0.08

7.2.2 Fourier Transform Infrared Spectroscopy (FTIR) analysis

Fourier transform Infrared (FTIR) technique has been employed to study the presence of various functional groups and change in vibrational bands due to the doping of Eu^{3+} at the Sn^{4+} site in Sr_2SnO_4. FTIR spectrum of the synthesized powders recorded in wavenumber range of 400-4000 cm^{-1} are shown in Figure 7.3. As discussed in Chapter 3, two characteristics bands observed at 502 cm^{-1} and 726 cm^{-1} belongs to vibrational modes of Sr-O and Sn-O_6 respectively [205]. The change in the position of these characteristics bands indicates incorporation of Eu at Sn-site. The vibrational band of Sn-O_6 stretching mode has shifted towards lower wavenumber side with increasing concentration of Eu. This band is observed at 708.54, 706.14, 705.27, 704.42 and 701.56 cm^{-1} for samples SSE1, SSE2, SSE4, SSE6 and SSE10 respectively. The shift towards lower wavenumber of Sn-O stretching mode is either due to difference in the atomic mass of host (118.71 amu) and substituted ion (152 amu) or due to change in lattice parameter. Moreover, it is further observed that there is no change in the position of mode corresponding to Sr-O band which further insure the incorporation of Eu specifically at Sn site. Additionally, a weak band observed at 856 cm^{-1} is corresponding to $SrCO_3$ vibrational frequency which may be possible on account of adsorption of CO_2 on the surface of samples.

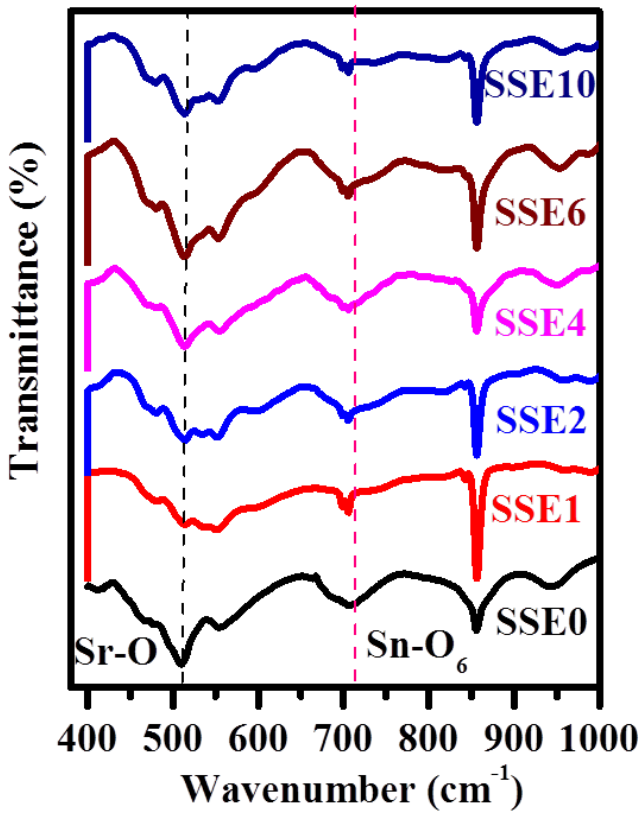

Figure 7.3 Room temperature Fourier transform infrared (FTIR) spectra of all samples.

7.2.3 Microstructural study using FESEM

The microstructural studies of sintered ceramic samples are carried out by recording their SEM micrograph of the fractured surfaces and shown in Figure 7.4 (a-f). The grains are spherical in shape with dense microstructure. The histogram of the distribution of grains is obtained by using "**Image J**" software. The Gaussian function is fitted to the histogram of all the samples is shown in Figure 7.5(a-f). Similar to crystallite size, the average value of grain size of Eu-doped samples is larger than undoped.

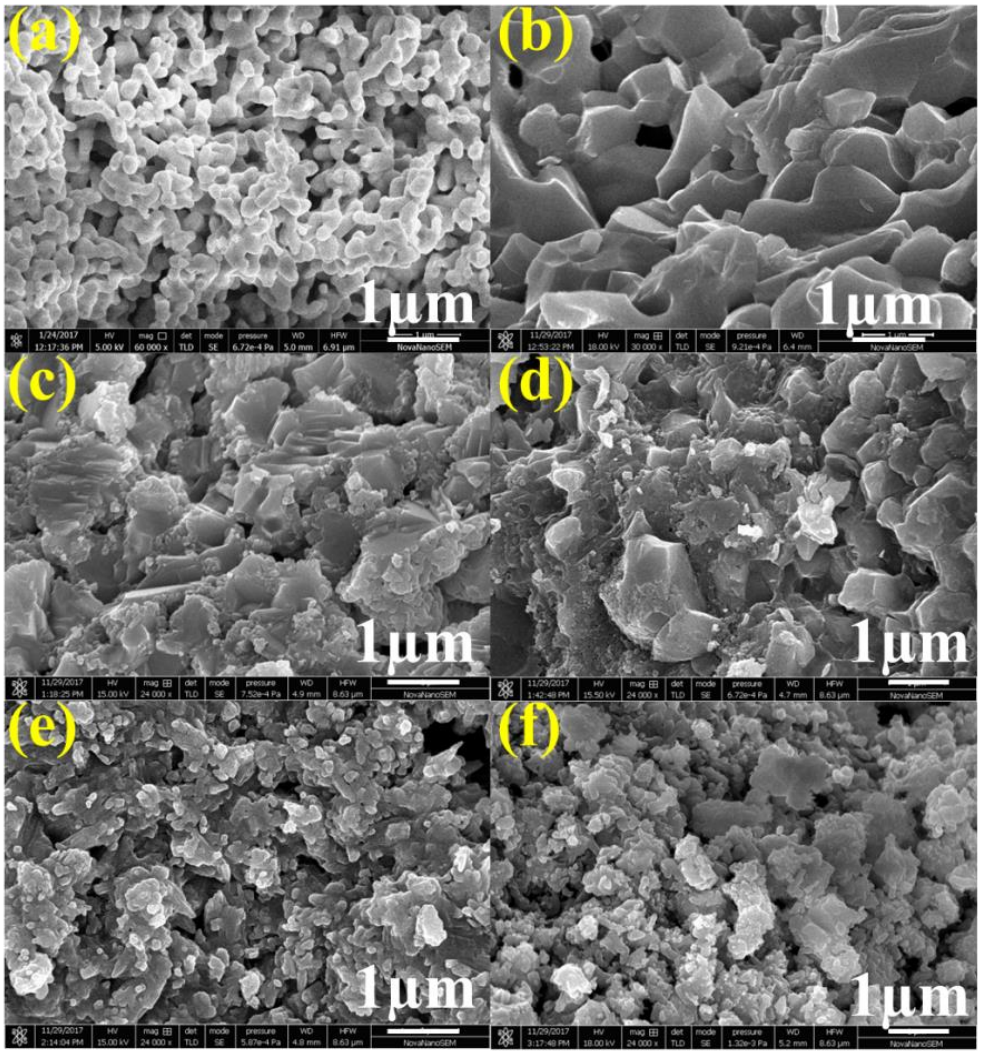

Figure 7.4 Field emission scanning electron micrograph (FESEM) of sintered samples (a) SSE0 (b) SSE1 (c) SSE2 (d) SSE4 (e) SSE6 (f) SSE10.

The degree of agglomeration between grains are observed for samples having Eu > 2 atom %, and gradually increases for above compositions SSE6 and SSE10 which decreases the grain size. Similar types of changes is already reported for Eu doped $BaTiO_3$ ceramics, in which they reported that the presence of agglomeration between the grains affect the grain growth process and reduce the grain size [65].

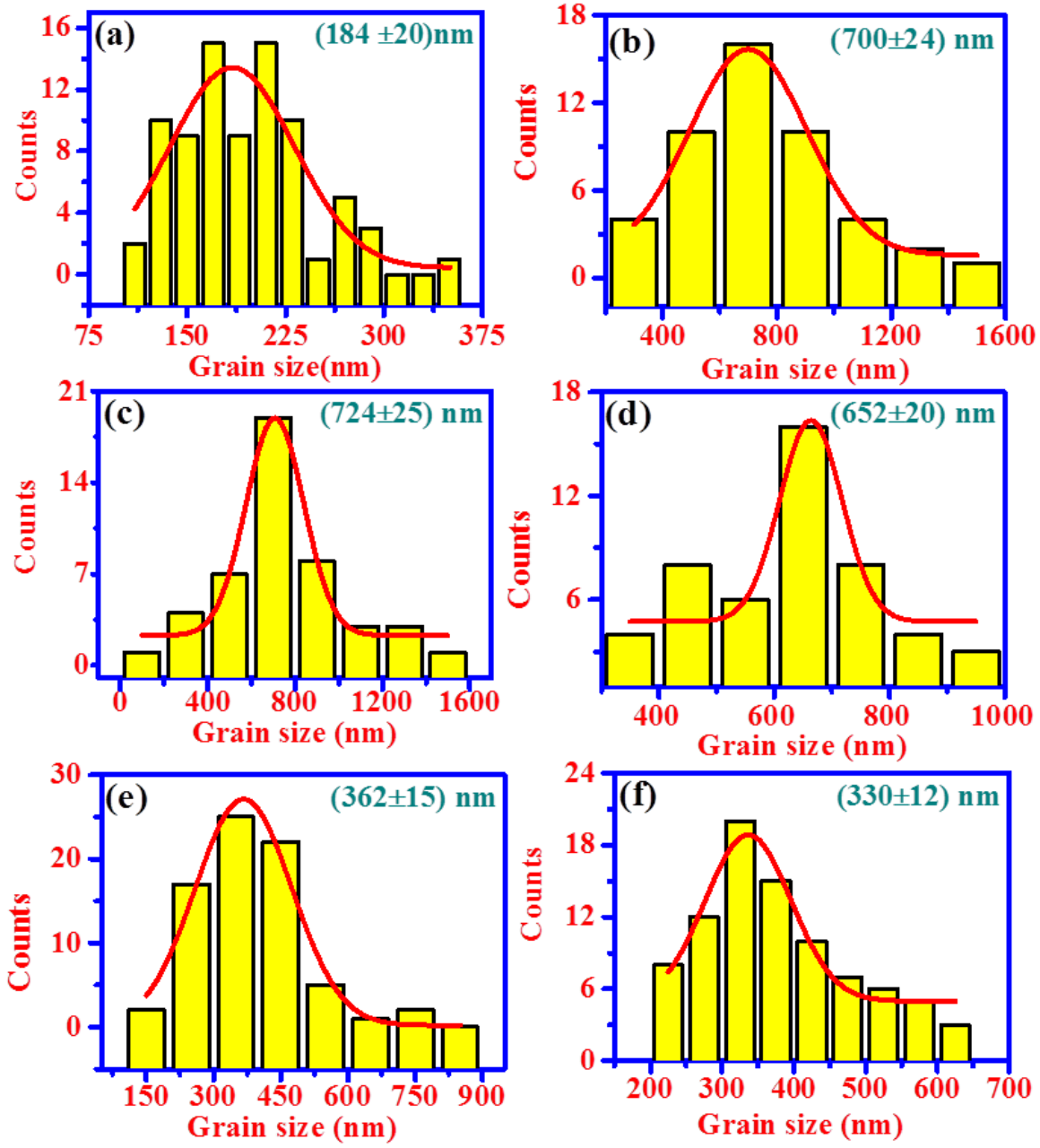

Figure 7.5 Histogram fitted with Gaussian function (a) SSE0 (b) SSE1 (c) SSE2 (d) SSE4 (e) SSE6 (f) SSE10.

7.2.4 X-ray Photoelectron Spectroscopy (XPS) analysis

To determine the valence state of elements present in the sample, X-ray photoelectron spectroscopic (XPS) technique has been employed. Survey scans plot of one of the sample $Sr_2Sn_{0.99}Eu_{0.01}O_4$ is shown in Figure 7.6(a). The HRXPS spectrum of Sr (3d) is shown in Figure 7.6(b), which shows double peaks centered at 132.9 and 134.5 eV corresponding to

states $3d_{5/2}$ and $3d_{3/2}$, respectively. Spin–orbit splitting energy of 1.60 eV confirms the presence of Sr in Sr^{2+} state in the samples. Figure 7.6(c) shows the HRXPS spectrum of Sn (3d), the double peaks centred at 486.03 eV and 494.13 eV are assigned to $5d_{5/2}$ and $5d_{3/2}$ states, respectively. The asymmetry in both the peaks is observed towards lower binding energy, which might be due to presence of Sn in more than one valence state. Deconvolution of the peaks have been carried out with the best fit ($\chi^2 < 3$), the position of the peaks in $3d_{5/2}$ state is 485.20 eV and 486.10 eV in $3d_{3/2}$, while the position of peaks in $3d_{3/2}$ state is at 493.60 eV and 494.50 eV. The spin-orbit splitting energy in both the peaks is 8.4 eV. The peaks observed at lower binding energy are assigned Sn^{2+} state of Sn while peak present at higher binding energy is assigned to the Sn^{4+} states of Sn, respectively. Figure 7.6(d) depicts the HRXPS spectrum of O (1s), asymmetry of the peak towards higher binding energy side indicates the presence of various kinds of oxygen species in the lattice. In order to know about the oxygen species, the peak is deconvoluted into two peaks position at 530.50 and 531.70 eV and assigned to the lattice oxygen (O^{2-}) and oxygen vacancies ($V_o^{\cdot\cdot}$) respectively. The HRXPS spectrum of Eu 4d presents in the binding energy range 130-150 eV [282], while in same range the core level spectrum of Sr 3d is found in present case. Due to lower concentration of Eu in $Sr_2Sn_{0.99}Eu_{0.01}O_4$, it cannot be detect in XPS spectrum of sample. Further, Eu can be probed by other technique discussed in following sections.

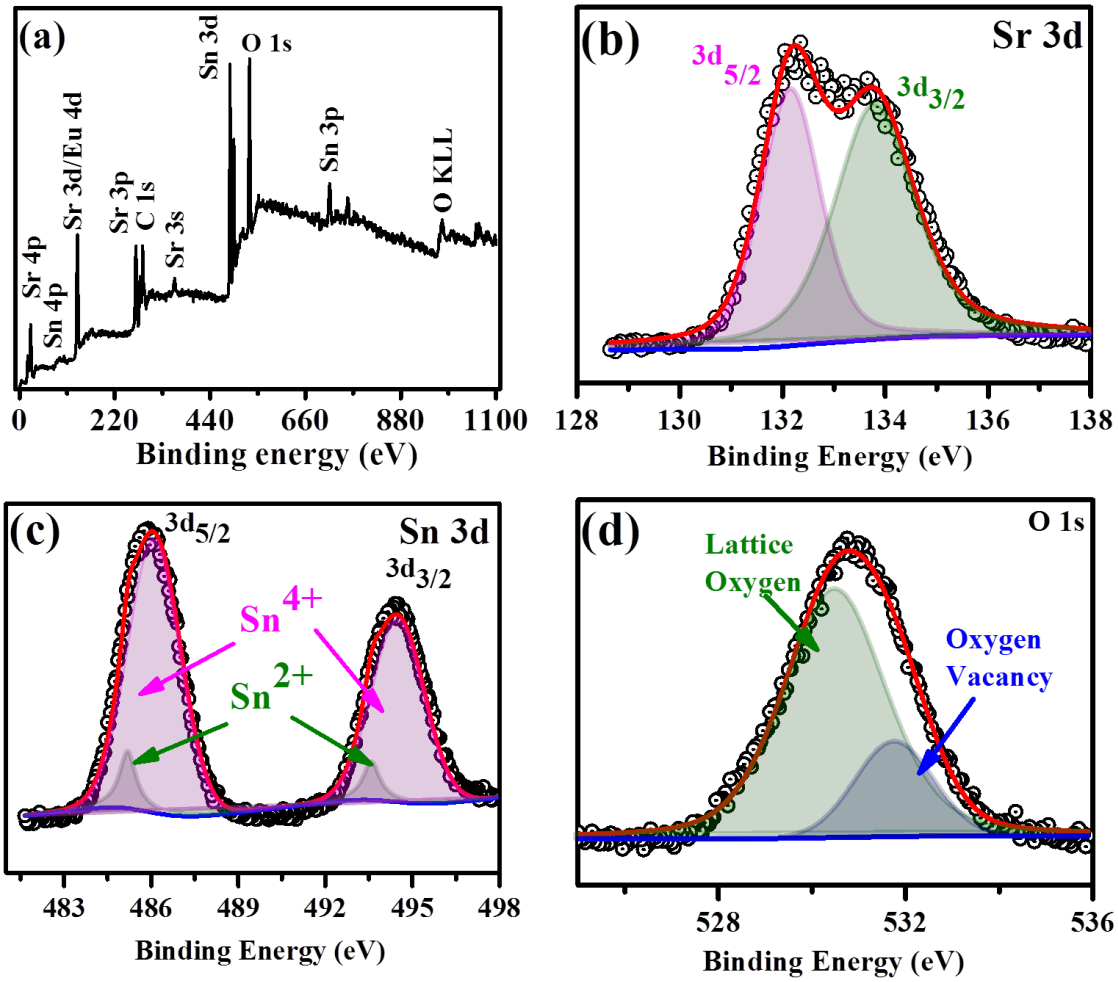

Figure 7.6 (a) Survey scan report of $Sr_2Sn_{0.99}Eu_{0.01}O_4$, Core level XPS spectra of (b) Sr 3d (c) Sn 3d (d) O 1s.

7.2.5 UV-Visible Spectroscopy

The UV-Vis absorption of all the samples is recorded in wavelength range 200-800 nm and illustrated in Figure 7.7 (a). A broad absorption band within 200-350 nm is observed in the spectrum of the entire sample. The absorption wavelength has been determined by extrapolating their edges to the wavelength axis, where absorption is 0. All the samples show significant transparency in wavelength range from 350-800 nm. The absorption coefficient in the wavelength 200-250 nm of samples increases with increasing Eu, which makes them suitable candidate for UV-detector application. Further, it is noticed that absorption edge shift

towards higher wavelength side by incorporation of Eu in the lattice, i.e., red shift which might be due to formation of charge transfer band O^{2-}-Eu^{3+} state [137].

The optical band gaps of all the samples are determined using Tauc plot given by Eq. (2.21). The Tauc plots for all samples are illustrated in Figure 7.7 (b-f). The linear region of the curve extrapolated on the energy axis where $(\alpha h\vartheta)^m = 0$ gives the value of direct $(m = 2)$ and indirect band gap $\left(m = \frac{1}{2}\right)$. The obtained values of direct and indirect band gap are given in Figure 7.7 (b-f). The direct band gap of the Eu- doped samples were found to be higher as compared to undoped one as discussed in Chapter 3. Further, it is noticed that the direct band gap of the samples has decreased with increasing Eu concentration from SSE1 to SSE10. However, on the other side the indirect band gap of samples was found to increase. The charge compensation mechanism is taken into account to understand this variation. Presence of oxygen vacancies in these samples has been already discussed in XPS technique. The defects present in the sample may form their own band within the band of sample [212]. Presence of these intermediate bands may be responsible for indirect band gap. As concentration of Eu increases it favours the formation of oxygen vacancies which populates this band which leads to increase the width of band due to presence of columbic force between these energy levels [283]. Due to this, the indirect band gap is increased. It is noticed from Table 7.1, that the crystallite size increases with concentration of Eu. Earlier, it is mentioned for many ceramics that the band gap decreased with increasing the crystallite size due to Burstein Moss effect acts in between the defect state and conduction band which is attractive in nature [212].

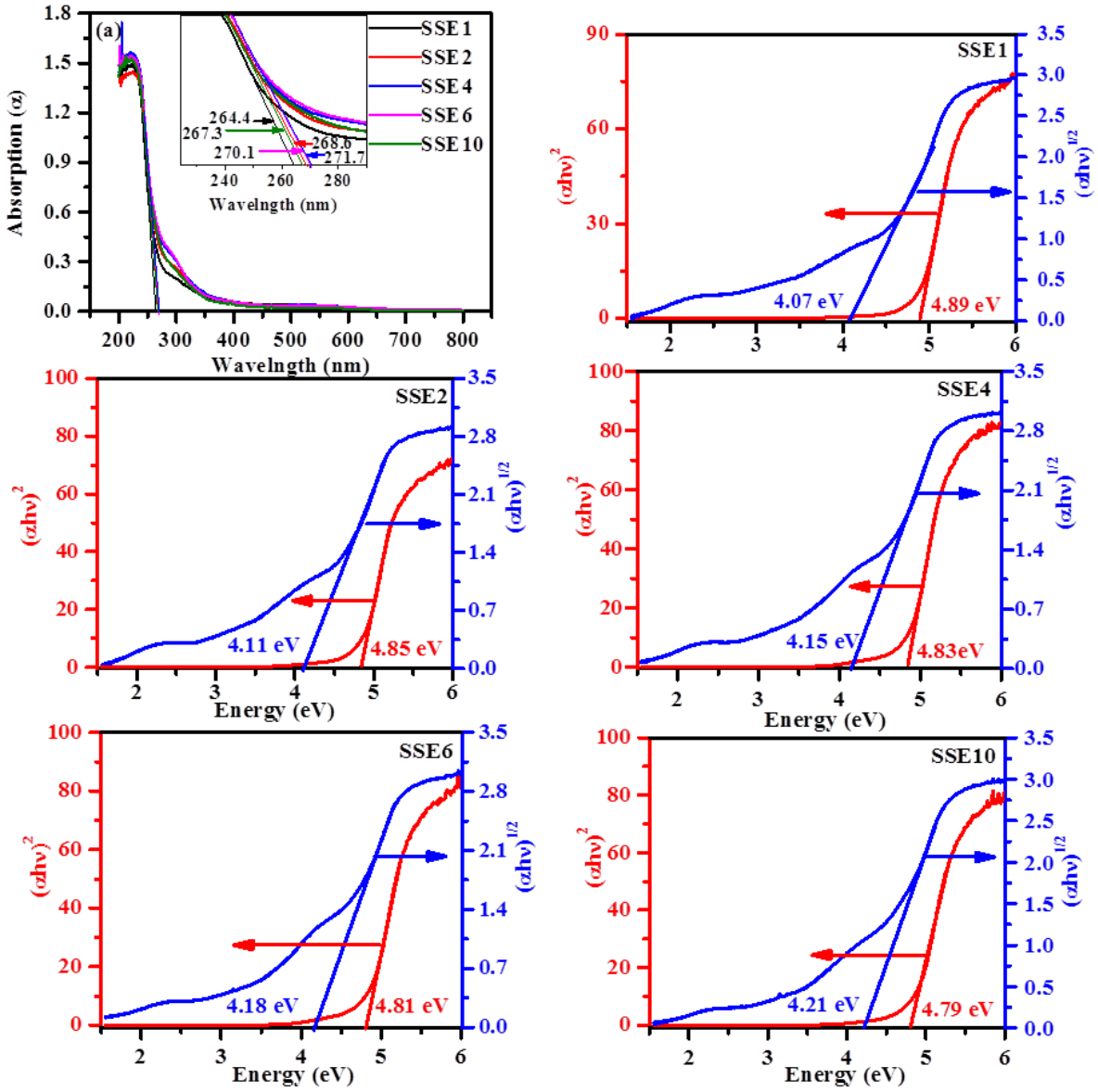

Figure 7.7 (a) UV-Vis spectra of all samples (b-f) Tauc plot generated from absorption for both direct and Indirect Band gap.

7.2.6 Photoluminescence Spectroscopy

Photoluminescence (PL) properties need to be studied to probe the defect state and their contributions in the application of optical devices, display devices etc. Before studying their emission properties first the excitation spectrum of the samples are recorded and shown in Figure 7.8(a). The excitation spectrum of the sample SSE4 shows five sharp peaks observed at 366 nm, 386 nm, 395 nm, 420 nm and 466 nm for emission at 614 nm [182]. These

transition peaks are arising due to transitions from $^7F_0$ energy level of Eu^{3+}. The strongest transition to the observed at 395 nm and 466 nm belongs corresponding to characteristic transitions $^7F_0 \rightarrow {}^5L_6$ and $^7F_0 \rightarrow {}^5D_2$ of Eu^{3+}. The highest intensity observed at 466 nm is used to record PL spectra of all samples. Figure 7.8(b) depicts the photoluminescence spectra in wavelength range 520-700 nm.

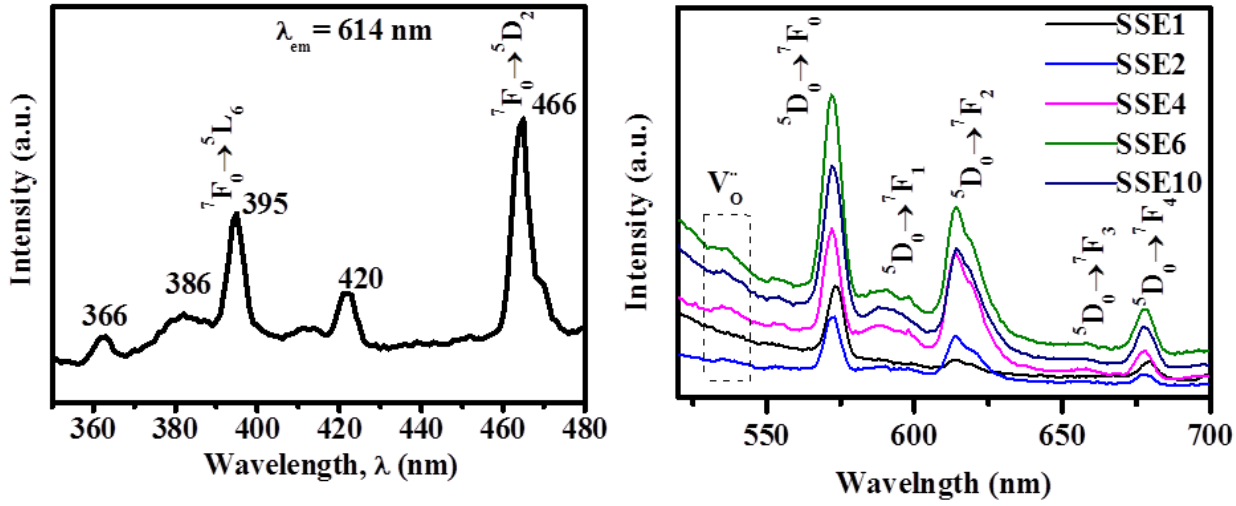

Figure 7.8 (a) Excitation spectra of a reference sample SSE4 for emission $\lambda_{em} = 612\ nm$ (b) Emission spectra of all samples under excitation wavelength $\lambda_{exc} = 466\ nm$.

The emission spectra of all samples contained various peaks at 572, 595, 614, 658 and 678 nm. All the emission peaks belongs to the characteristic transition of Eu^{3+} between the energy levels $^5D_0 \rightarrow {}^7F_{0,1,2,3,4}$ of Eu^{3+} respectively. There is one more peak observed at 535 nm which does not belong to transition of Eu^{3+}. From literature, it is found that this transition peak is originated by transition from oxygen vacancies [182]. The XPS of O 1s indicates the presence of oxygen vacancy in the sample SSE1, which further suggests that the transition observed at 535 nm is originated from oxygen vacancy. There are more reports are available on Eu doped at Sr-site of Sr_2SnO_4 such that, Sunao Kamimura et al. reported that Eu incorporation at the Sr-site in Sr_2SnO_4 shows the purple photochromism due to presence of vacancies of Sr [137]. Xiaochun Zhou et al. studied the phosphor properties of Eu doped

Sr_2SnO_4 and reported that it can be used as red phosphor material [137]. There are also other reports are available on Eu doping in alkaline orthostannate (M_2SnO_4: M=Ca, Sr, Ba) which shows that the PL spectra of samples have most intense peak at 614 nm and it can be used as a potential candidate for optical device applications [131, 202, 284–288].

The PL spectrum of samples in present case show two most intense transitions observed at 572 nm and 614 nm which belongs to transition $^5D_0 \rightarrow {}^7F_0$ and $^5D_0 \rightarrow {}^7F_2$ respectively. The transition $^5D_0 \rightarrow {}^7F_0$ for Eu doped Sr_2SnO_4 is not reported in literature till now. Although, presence of this transition $^5D_0 \rightarrow {}^7F_0$ in various oxides ($Y_2O_3:Eu^{3+}$, $ZnO:Eu^{3+}$, $Gd_2Hf_2O_7:Eu^{3+}$) and halides phosphor material is not surprising us [289–293].

The origin of transition $^5D_0 \rightarrow {}^7F_0$ is under debate, while the other two transitions $^5D_0 \rightarrow {}^7F_{1,3}$ and $^5D_0 \rightarrow {}^7F_{2,4}$ are allowed by selection rule of magnetic dipole transition and electric dipole transition respectively. The transitions within 4f shells of rare earth ions are well explained by Judd-Ofelt theory. In this theory, the electric dipole transition between various states of the $4f^n$ shell is assumed to be partially allowed by mixing the higher configuration of opposite parity into $4f^n$ shell. In this configuration the odd parity crystal field potential and their closure approximation has been used. There are two probable reasons for this forbidden transition which are discussed in literature [289];

(i) Due to mixing of a high lying odd parity state for which the closure approximation is not well applicable. Since the wave function corresponds to $^7F_0$ is mixed into the $^5D_0$ states considerably by the spin orbit interaction. The electric dipole transitions allowed between the state $^7F_0 \rightarrow {}^5D_0$ due to mixing of an odd parity state through the linear term of crystal field potential.

(ii) The second reason is that it borrow the intensity from the transition $^5D_0 \rightarrow {}^7F_J$ (J=2, 4, 6, etc.). The j-mixing effect describes the participation of the $^7F_2$, $^7F_4$ and $^7F_6$ states in the final

composition of the $^7F_0$ state. Since the observed transition $^5D_0 \rightarrow {}^7F_2$ state is hypersensitive transition, whose intensity varies enormously with increasing the chemical content of Eu^{3+}.

Since $^7F_{2,4}$ state is one of the most favourable state which involved in the final composition of $^7F_0$ and the allowed transition takes place via the j-mixing state of electric dipole transition. In present case, both the reasons are valid and might be responsible for the presence of $^5D_0 \rightarrow {}^7F_0$ transition. The Eu^{3+} acts as acceptor at Sn^{4+} site of Sr_2SnO_4 and the charge compensation mechanism takes place according to Eq. (7.1). The PL spectrum of all samples contained a weak intensity peak observed at 535 nm. The position of this energy level is just above the energy level of transition peak $^5D_0 \rightarrow {}^7F_0$ as shown in Figure 7.9(a). These two energy level is very close to each other, then possibility of transfer of charge from oxygen vacancy to $^5D_0 \rightarrow {}^7F_0$ can not be ruled out. According to Dexter theory, an efficient energy transfer (ET) requires a spectral overlap between the donor emission and the acceptor excitation [294]. From PL spectra it is observed that the ET takes place from oxygen vacancies to the energy level $^5D_0 \rightarrow {}^7F_0$ is due to increasing oxygen vacancies with Eu concentration, which tries to be overlap with the $^7F_0$ state. In addition to ET from oxygen vacancies the resultant emission is shifted from red to green region (577 nm).

The increase in intensity of PL peaks corresponding to transition $^5D_0 \rightarrow {}^7F_J$ are observed with increasing the concentration of Eu^{3+} which may be because of increase in the associated energy levels. In order to probe the effect of Eu^{3+} in the emission spectrum, the ratio of the integrated area of PL intensity peaks have been calculated for transitions $^5D_0 \rightarrow {}^7F_0$ to $^5D_0 \rightarrow {}^7F_2$, termed as I_{02} and for $^5D_0 \rightarrow {}^7F_1$ to $^5D_0 \rightarrow {}^7F_2$, termed as I_{12} and given in Table 7.1. The numerical value of the ratio I_{02} is gradually increases from 0.013 (SSE1) to 1.06 (SSE6) and then decreased to 0.98 (SSE10), while value of I_{12} gradually decreases from 0.19 (SSE1) to 0.08 (SSE10). From this variation, the optimum concentration of Eu in SSE sample is found to be 6% which is also known as critical concentration. The further increase of Eu

leads to decrease in luminescence intensity which termed as concentration quenching. The concentration quenching effect has occurred due to the non radiative energy transfer between Eu^{3+}-Eu^{3+} ions [295].

In order to probe the effect of the dopant on the overall intensity of the emission the CIE coordinate for PL emission has been calculated. The calculated value of CIE coordinate were indexed for every sample in the commission international del-Ec lairage (CIE) chromaticity diagram shown in Figure 7.9(b). From this diagram, it is observed that the most dominated transition of the samples were shifted towards green region because of the energy transfer from oxygen vacancies and $^7F_{2,4}$ to $^7F_0$ energy level.

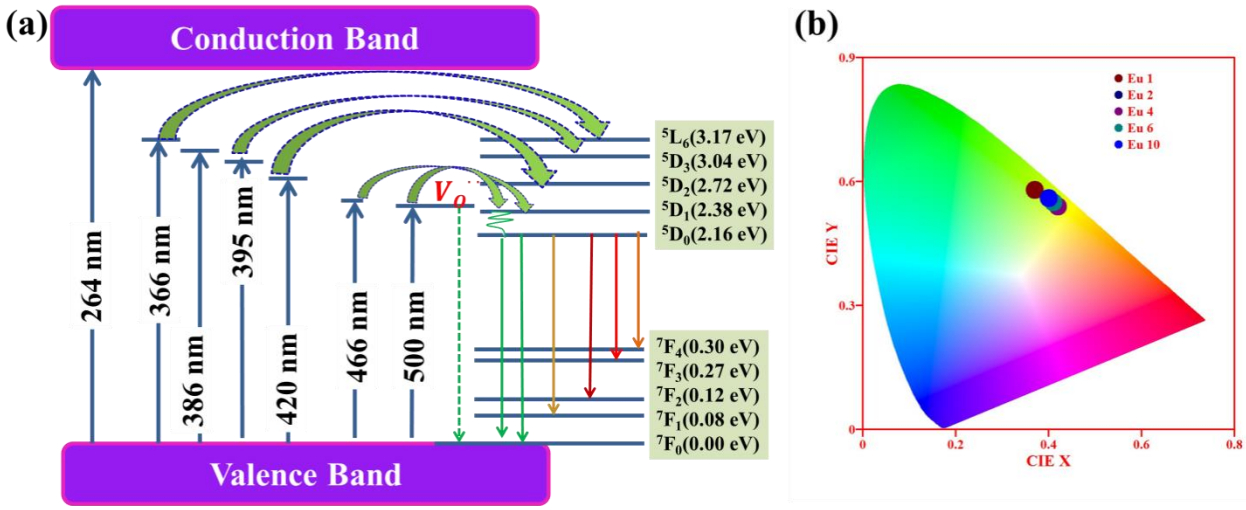

Figure 7.9 (a) Energy band diagram of Eu-doped Sr_2SnO_4 sample (b) CIE coordinate of all sample.

7.2.7 Life-time measurement

PL studies have suggested the energy transfers are takes place between level oxygen vacancies ($V_{\ddot{O}}$) observed at 535 nm to $^5D_0 \rightarrow {}^7F_0$ observed at 572 nm. All the PL spectra of samples possess an intense red emission at 614 nm significantly contributed to $^7F_0$ state. To confirm this energy transfer between energy levels, the life time of associated energy levels recorded using excitation wavelength 466 nm for 535 nm, 572 nm and 614 nm respectively,

are shown in Figure 7.10(a-c). The original experimental decay curve is fitted with the exponential decay function given by Eq. (7.2).

$$I = A \exp\left(-\frac{t}{\tau}\right) \qquad (7.2)$$

Where, I is the intensity, A is constant, t is time and τ is the decay time. Decay curve obtained for all the samples are fitted with the function as given by Eq. (7.2). The perfect fitting of experimental data with Eq. (7.2) indicates that the transition occurring from these energy levels are singlet state. The calculated decay times for the decay curve for all samples are shown in Figure 7.10(d). From Figure 7.10(d), it is found that as concentration of Eu increases the life time of energy level of oxygen vacancy decreases upto SSE6 and almost constant for SSE10. However, the decay time for 572 nm and 614 nm are increased with composition of Eu upto SSE6 and then decreased for SSE10. The decrease in life time above SSE6 reconfirms that the critical concentration of Eu is 6% in Sr_2SnO_4. Discussion for sample SSE6 has been made because for this sample highest energy transfer is observed. For sample SSE6, the life time for 535 nm was 3.1 ms, for 572 nm 7.6 ms and for 614 nm 7.9 ms, the almost similar life time for 572 nm and 614 nm clearly indicated that the population of both energy levels was almost equivalent. With increasing Eu, oxygen vacancies also increases and populate the associated energy level. As energy level of oxygen vacancies increases it trying to overlap with the most closely state of Eu^{3+} which is observed at 572 nm. The overlapping between these states results an efficient energy transfer between both energy levels by a well stabilised theory Dexter theory [294]. Due to energy transfer between these energy levels the life time of energy level of oxygen vacancy is decreased. Same phenomenon is applied to all samples.

Several authors showed that the phosphors with short luminescence decay time are suited more as compared to the long decay phosphors for application point of view in modern day flat panel display devices [131].

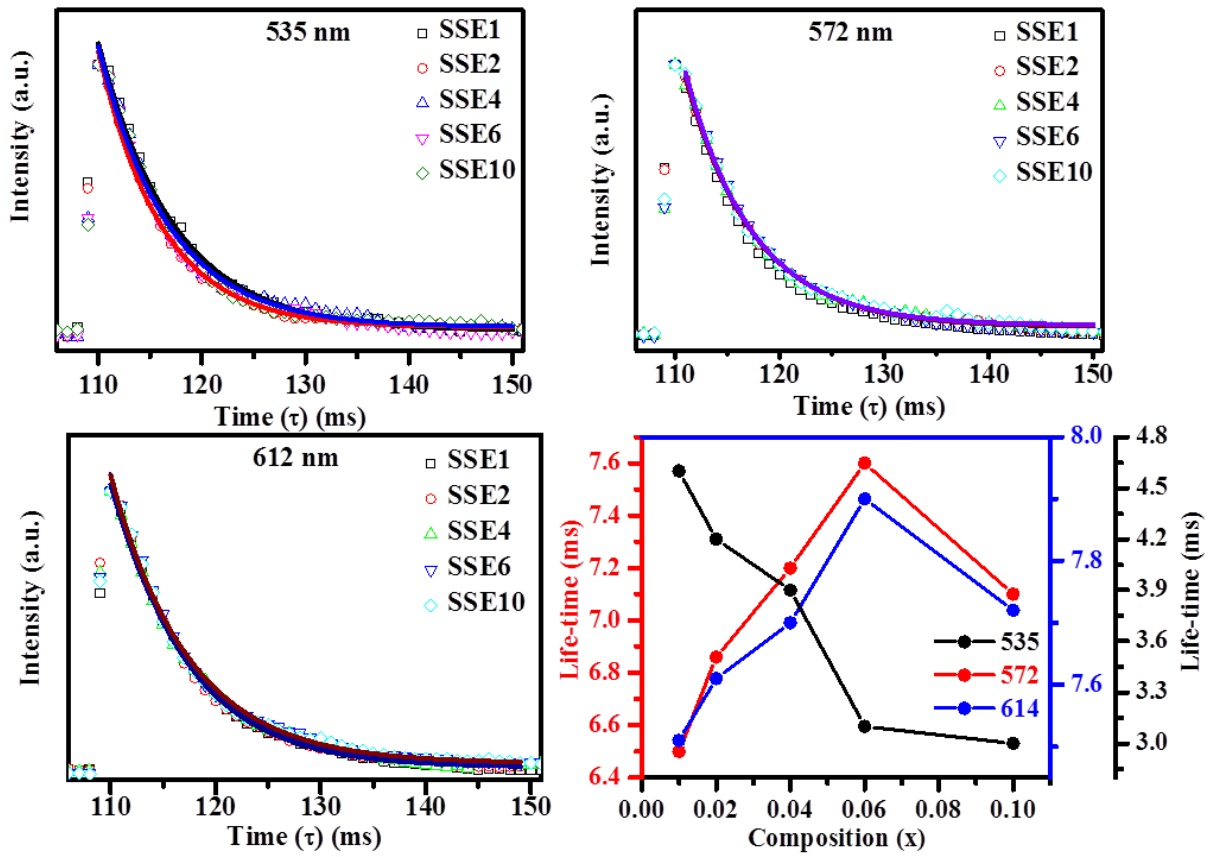

Figure 7.10 Decay time curve for wavelength (a) 535 nm (b) 572 nm (c) 614 nm (d) Variation of life time with composition.

7.3 Conclusion

The single phase solid solution of compositions $Sr_2Sn_{1-x}Eu_xO_4:xEu^{3+}$ with x= 0.01, 0.02, 0.04, 0.06, 0.10 were successfully synthesized via conventional ceramic route. Further, the incorporation of Eu^{3+} has been studied from X-ray diffraction, Rietveld refinement and FTIR spectroscopy. The optical absorbance of all samples shows red shifts in the band edge with the incorporation of Eu^{3+} in the sample. The PL of the Eu doped samples were studied under excitation wavelength 466 nm. The various characteristics emission peaks of Eu^{3+} were observed for Eu doped samples $^5D_0 \rightarrow {}^7F_J$ (J=0, 1, 2, 3, 4). The ratio of integrated peak area from transition J=0 to J=2 termed as I_{02} and I_{12} for J=1 to J=2. Increase in value of I_{02} and I_{12} from SSE1 to SSE6 and decreased for SSE10 are observed. The energy transfer has been studied by decay time. Decay time for oxygen vacancy observed at 535 nm is lower, while it

is equivalent for transition observed at 572 nm and 614 nm. The energy level of oxygen vacancy and 572 nm is very close to each other and due to overlapping between these states results an efficient energy transfer between these energy states. Due to energy transfer from 535 nm to 572 nm, resultant emission is shifted towards green region. The concentration quenching is observed for the composition $x>0.06$. The emission in visible range with short decay time makes it a promising candidate for optical device and for bio-imaging applications.